Supporting Information

S1 Additional information about the inputs of our modelling framework

The geographical input used for the three domains of our model is obtained from the modified International Geosphere-Biosphere Programme global land cover classification, and relies on data from the Moderate Resolution Imaging Spectroradiometer (IGBP-Modified MODIS; Friedl et al. (2010)). The resulting IGBP-Modified MODIS database has a resolution of 30 arc seconds (approx. 1 km) and can provide 20 land-cover categories that are mainly related to different types of vegetation (e.g., evergreen forest, mixed forest). However, the IGBP-Modified MODIS database, as well as other common geographical databases, has only one land-use category defined for urban areas.

The meteorological initial conditions and lateral boundary conditions are obtained from ERA5, the fifth-generation reanalysis produced by the European Center for Medium-Range Weather Forecasts (ECMWF). In ERA5, a variety of observations from more than 20 satellites, radiosondes, aircraft measurements, etc. have been combined and assimilated (Hersbach et al., 2020). ERA5 provides hourly meteorological fields with a horizontal resolution of 31 km and 137 vertical model levels from the surface up to 0.01 hPa (as available via the Copernicus Climate Change Service, https://www.ecmwf.int/en/forecasts/datasets/reanalysis-datasets/era5).

The initial and lateral boundary conditions for our simulated concentration fields are from experiment gznv of the Integrated Forecasting System (IFS) Cycle 45r1. This simulation has been implemented by ECMWF and is a key part of the Copernicus Atmosphere Monitoring Service (CAMS, as available via Atmosphere Monitoring Service, https://confluence.ecmwf.int/pages/viewpage.action?pageId=116963341). The IFS Cycle 45r1 provides 6-hourly estimated mixing ratios of CO_2 and CH_4 with a horizontal resolution of approx. 40 km (following the N256 reduced Gaussian grids from ECMWF) and a vertical resolution of 137 levels (Browne et al., 2019; Rémy et al., 2019).

S2 Improved VPRM

As mentioned in Sect. 2, the CGLS-LC100 land cover map has been used to refine the vegetation classification over the innermost domain. Figure S1 shows the refined map of the domain using CGLS-LC100 (left), the original map classified with SYNMAP (middle) and the difference between the two maps (right). As seen in the middle plot, the original map shows no vegetation type classified in the middle of the domain, i.e., the city of Munich. After our refinement, more vegetation types can be recognized inside the city of Munich. Table S1 shows the details on how the Copernicus classes were reclassified into the eight vegetation fraction classes used in the VPRM preprocesser.

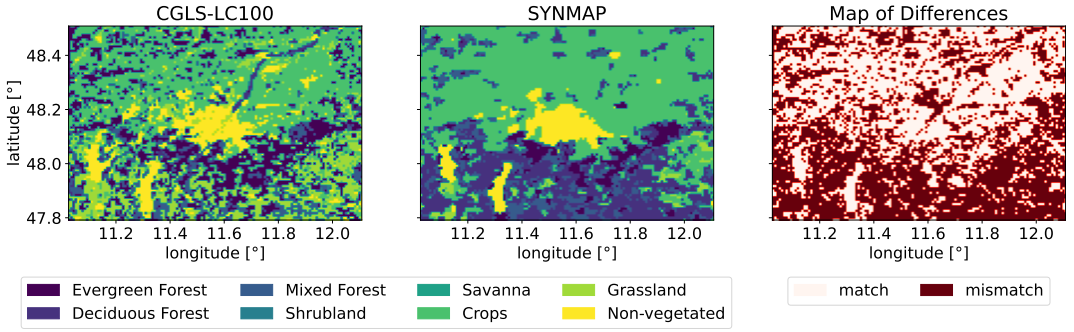

Figure S1. The maps of the vegetation classification with (left) and without (middle) refining using CGLS-LC100, and their difference (right).

S3 EU Local Climate Zones (LCZ) map

The EU LCZ map used in our study was generated with the protocol supported by the World Urban Database and Access Portal Tools project (WUDAPT, as available via http://www.wudapt.org/). The LCZ classifications are used for distinguishing different types of landscapes, which include ten land-cover types defined for urban areas (e.g., compact high-rise, compact low-rise), and another seven land-cover types for vegetation types that are not used in our model. The LCZ classification is illustrated in Fig.1 of Demuzere et al. (2019). In terms of WUDAPT, the morphological urban features are captured within multi-spectral images from satellites (e.g., Landsat 8). Moreover, the LCZ types for the targeted area are identified by a random forest classifier (See et al., 2015). For our study, we extracted the area of our innermost domain from the full EU LCZ map (Demuzere et al., 2019). Then the morphological information from this clipped LCZ map was extracted and transformed into the format used in the WRF pre-processor (Brousse et al., 2016).

S4 Relevant information regarding TNO_GHGco_v1.1

S4.1 Vertical emission profiles for point sources

The vertical emission profiles for point sources we use in our study are provided by Bieser et al. (2011). We re-allocated the layers in this vertical emission profiles (see Fig. S2(a)) to the model layers of of model. The re-allocated vertical profiles for point sources are shown in Fig. S2(b).

S4.2 Reclassification of the GNFR categories in TNO_GHGco_v1.1

As described in Sect.2 of the main text, TNO_GHGco_v1.1 follows the GNFR sector classifications (Super et al., 2020). We aggregate eleven emission sectors from GNFR (see the categories in the legend of Fig. S2) to five major sectors applied in different tracers of our model. The details on the aggregation are shown in Table S2 for CO_2 and Table S3 for CH_4.

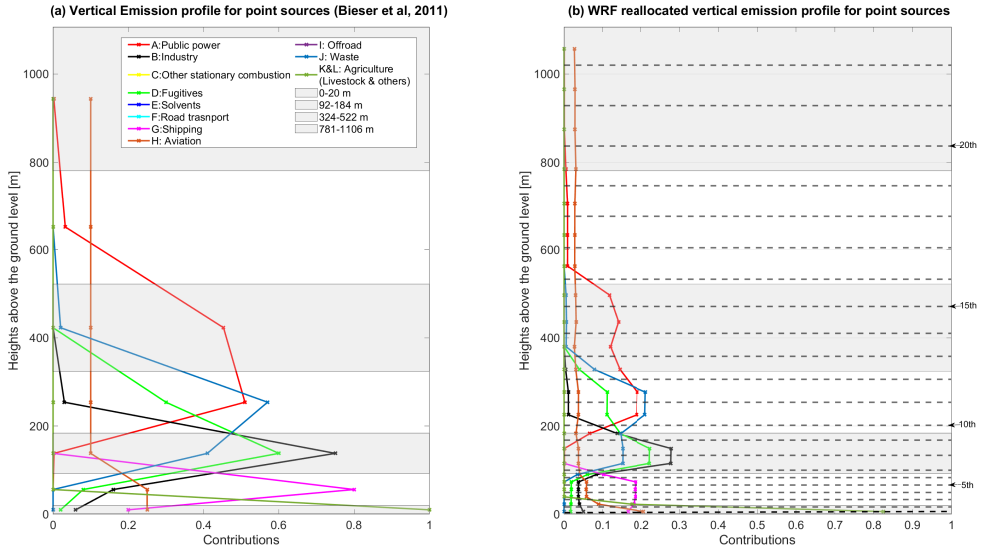

Figure S2. Vertical emission profiles for point sources (a) from Bieser et al. (2011) are re-allocated to our WRF vertical layers (b). The alternating gray and white background stands for the seven vertical layers used by Bieser et al. (2011). The dashed lines in (b) delimit the first 22 vertical layers above the ground in our WRF setup.

S5 Comparisons of other meteorological variables

Expanding on Sect. 3 of the main text, here we discuss plots comparing our model wind fields to DWD measurements and our modelled temperature and precipitation to measurements from LMU and DWD.

S5.1 Wind comparison between the model and the DWD Munich Airport station

Figure S3 shows a comparison between the modelled and the measured values obtained from the DWD Munich Airport station (see Sect. 3 of the main text, where also Fig. 2 showed the measurements of the LMU station). As depicted in the wind roses of Fig. S3(a), the prevailing measured surface wind blows from the southwest, while the modelled directions show more variations. Mismatches of wind directions mainly appear during daytime, but the overall trends can be reproduced by the model (red crosses in Fig. S3(c); RMSE: 72 degrees and MAE: 17.83 degrees). In terms of wind speeds (see Fig. S3(b)), the model matches well with the measurements with a RMSE of 1.58 m/s and a MAE of 0.15 m/s. At nighttime, the measurement exhibits higher wind speeds under the same wind directions, compared to the model (see Fig. S3.((a.5) & (a.6)).

S5.2 Comparisons of other meteorological variables

Apart from the wind fields mentioned above, other meteorological parameters are also expected to impact the behavior of the tracers in our model. The temperature at a height of two meters above the ground (T2) plays a key role in calculating biogenic

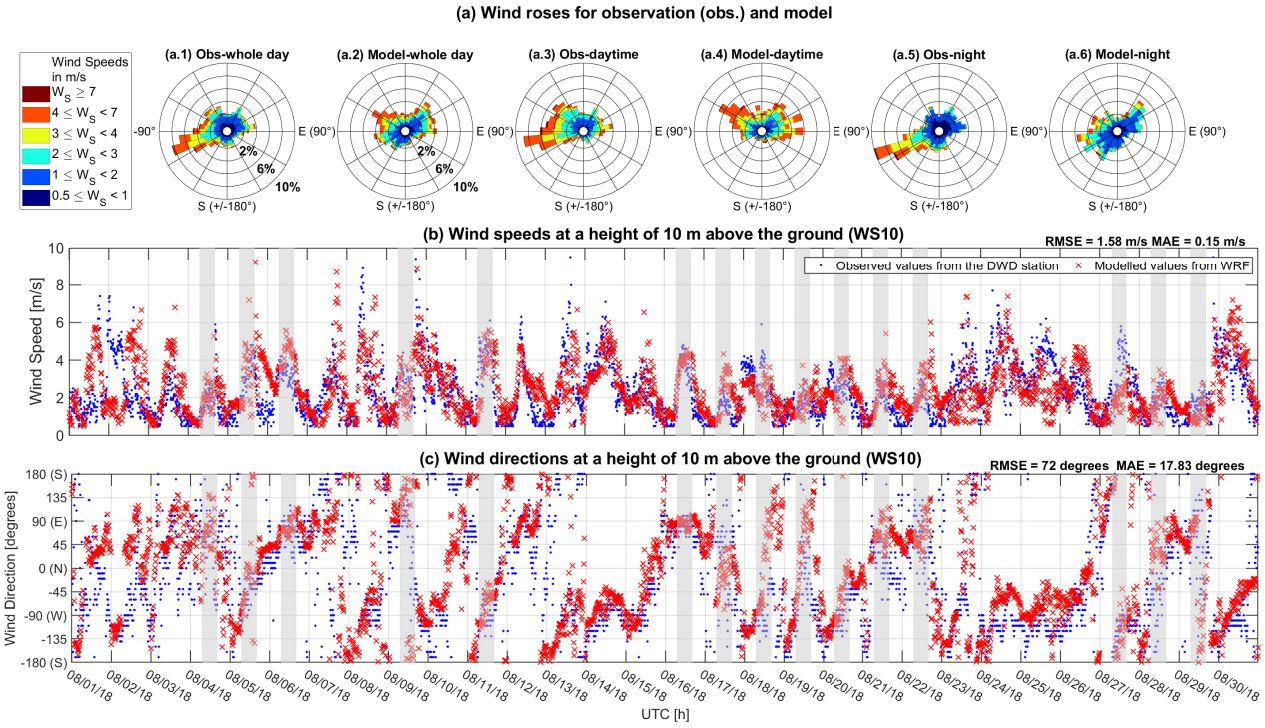

Figure S3. Wind roses (a) and time series of simulated and observed wind speeds (b) and wind directions (c) at a height of 10 m above the ground at Munich Airport (DWD station). Wind roses for the measurements over August 2018 are plotted in Panels (a.1): 24 hours, (a.3): daytime from 6 am to 5 pm only and (a.5): nighttime only, while Panels (a.2), (a.4) and (a.6) represent the modelled values. Each wind rose indicates WS10, WD10 and the frequency (% scale) of wind coming from a particular direction during the targeted period. The blue dots in Panels (b) & (c) represent the measured values from the DWD station and the red crosses represent the simulation. The grey shaded areas mark the measurement periods used for the model-measurement comparison of column concentrations in Sect. 4 of the main text.

fluxes in VPRM (Mahadevan et al., 2008). Precipitation is also an important point in assessing the model behavior, since the functionality of our instrument used for measuring the column concentrations is influenced by rainfall, as described in detail in Sect.4.1.

Figure S4 compares T2 and precipitation between models and measurements. Over the entire simulation period, the modelled T2 (black solid lines in Fig. S4(a) & (b)) shows trends similar to the measurements (red dashed lines) from both weather stations. As illustrated in Fig. S4(b), a better agreement appears to exist between the model and values from the LMU station, with a RMSE of 2.1 K and a MAE of -0.23 K, while the RMSE between the simulated values and those measured at DWD is 2.3 K, and the simulated values are generally higher (MAE: 1.15 K). During the daytime, the curves of the modelled and measured T2 generally match well, apart from the appearance of some peaks at noon measured by the LMU weather station (Fig. S4(b)). Major discrepancies of T2 between models and measurements occur during nighttime, at the early morning and at specific days, e.g., 10 and 24 August.

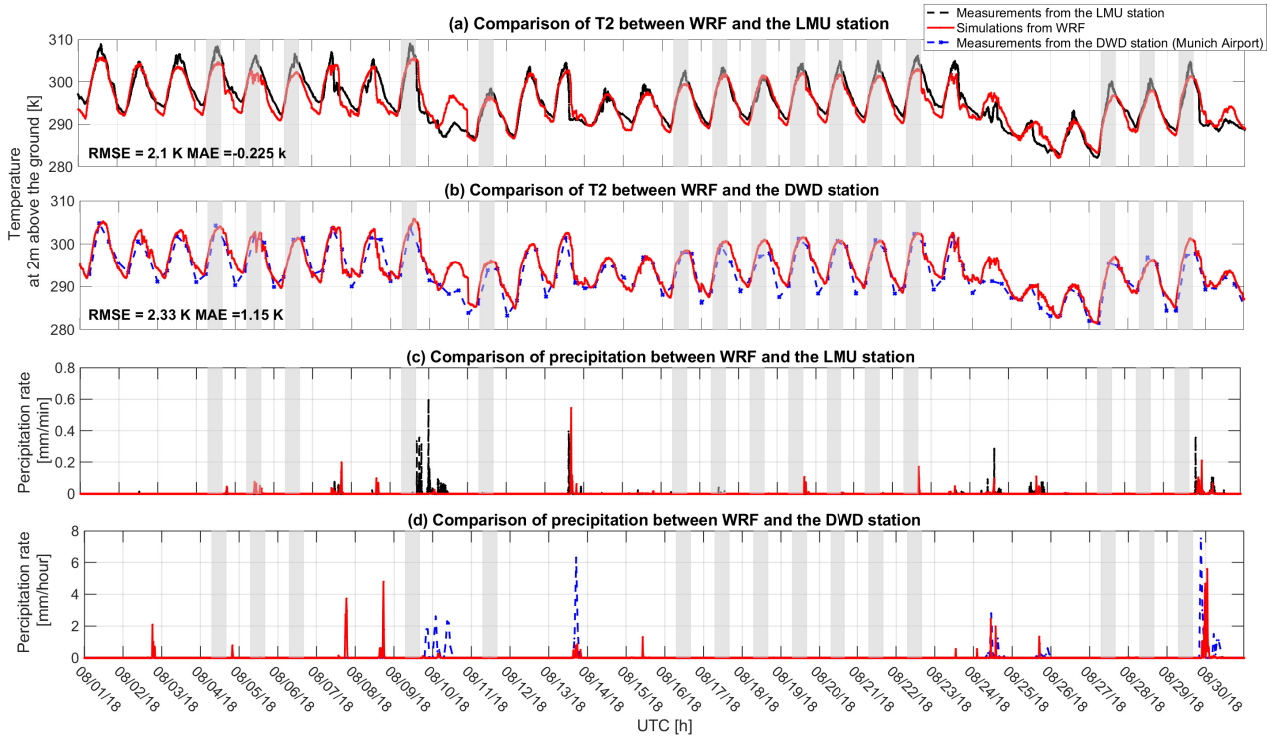

Figure S4. Comparison of temperatures at a height of 2 meters above the ground (T2; upper two panels) and precipitation values (lower two panels) between the model and two stations from 1 to 30 August, 2018: Panels (a) & (c) display data from DWD and Panels (b) & (d) show values from the LMU station. In all subplots, the simulations are plotted using the red solid lines while the measurements are represented by the blue dashed lines. The grey shaded areas mark the measurement periods used for comparing to the simulations in Sect.4.

One of the potential reasons for the discrepancies between models and measurements on these two specific days is that the mesoscale model can not reproduce the precipitation on these two days well, especially for 10 August. The missing or weak precipitation potentially led to unrealistic temperatures. As evident in Fig. S4(c & d), most of the rainfalls in August, 2018 can be replicated by the model, but the magnitude of the precipitation is not always well estimated. The disagreement in precipitation between the model and measurements can be due to several potential error sources. For instance, the spatial resolution of the mesoscale model may be not sufficient to fully reproduce complex flow features on the micro-scale or to resolve orographic uplift, but these effects can have an impact on the measurements (Collier et al., 2013).

S6 Measurement performance

The day-by-day measurement performance for our measurement campaign in 2018 is illustrated by Table S4 below. The criteria for the assessment in the table are based on studies for the Berlin region (Hase et al. 2015; cf. their Table 1) and for Paris (Vogel et al. 2019; cf. their Table 2). As a basic prerequisite, all the measurement sites should work, otherwise the overall

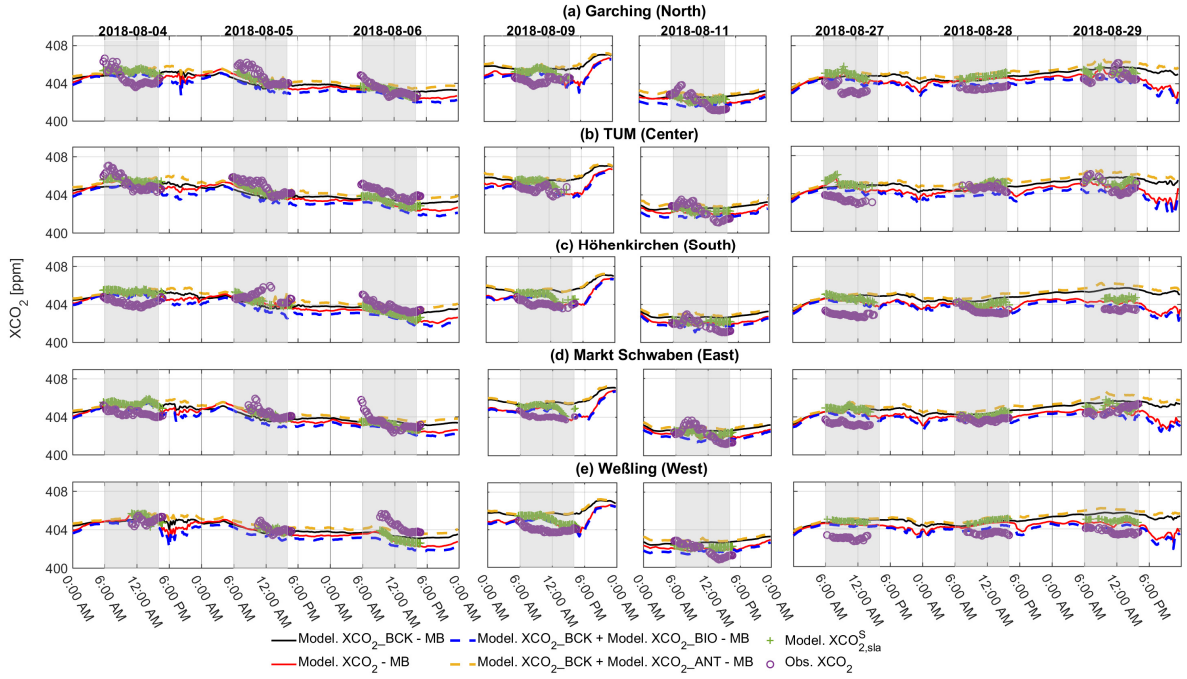

Figure S5. Modelled $\mathrm{XCO}^{\mathrm{S}}_{2,\mathrm{sla}}$, attribution of variations to different tracers, and the measurements at five sites of MUCCnet for the dates studied but not shown in Fig. 4 of the main text. The purple circles represent the column measurements from MUCCnet and the green '+' markers stands for the modelled $\mathrm{XCO}^{\mathrm{S}}_{2,\mathrm{sla}}$ after subtracting the MB. The other lines in the plot give pressure-weighted modelled column concentrations along the full time series. These are calculated following Eq. 1 of the main text (i.e. without smoothing using the SZA-dependent AK) and all corrected by MB. The black curve represents the modelled background XCO_2_BCK, and the red curve shows the modelled XCO_2. The dashed yellow and blue curves highlight the concentration changes caused by human activities (XCO_2_ANT) and biogenic activities (XCO_2_BIO). The grey shaded areas mark the measurement periods used for comparing observations to model results.

quality is set to be '+'. The overall quality levels are then determined from the observational coverage during one day: daily temporal coverage lower than 25%: '+'; from 25% to 50%: '++'; from 50% to 75%: '+++'; from 75% to 100%: '++++'. The observational coverage at more than three sites has to satisfy the criterion.

S7 Comparison between the model and the measurements for the rest of the selected dates

Figures S5 and S6 show the modelled and measured column concentrations of CO_2 and CH_4, with contributions from different tracers for the rest of the selected dates, complementary to Figures 4 and 5 in the main text.

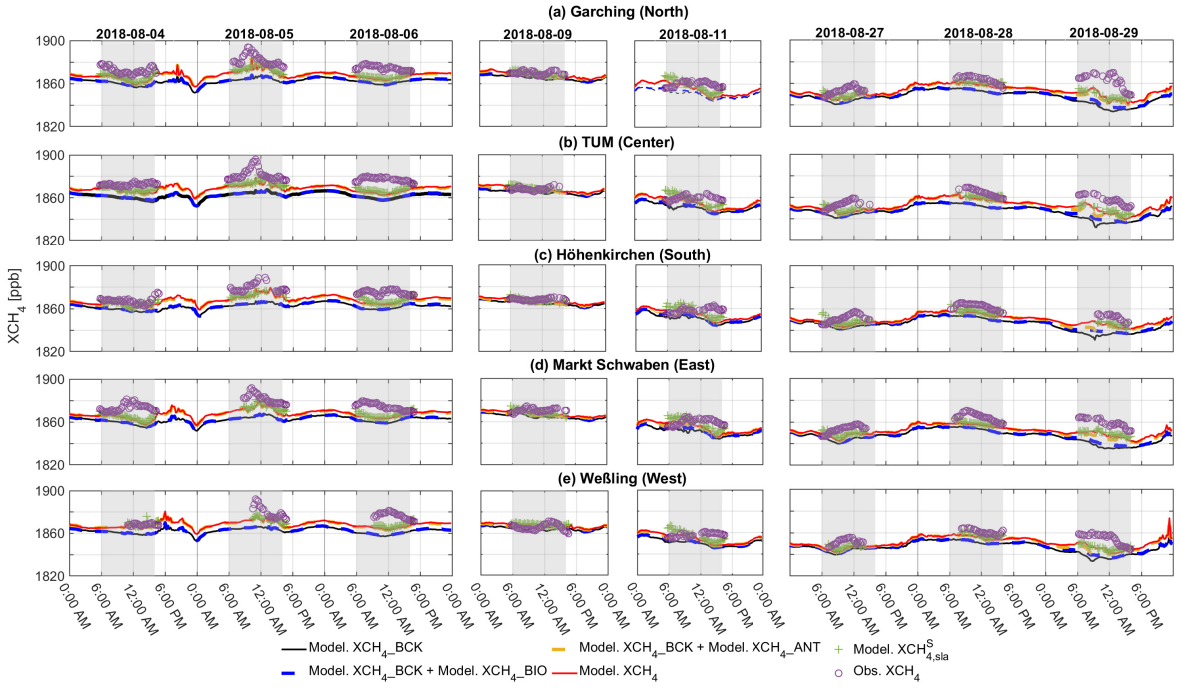

Figure S6. Modelled $\mathrm{XCH}_{4,\mathrm{sla}}^{\mathrm{S}}$, attribution of variations to different tracers and the measurements at five sites of the MUCCnet for the dates studied but not shown in Fig. 5 of the main text. The purple 'o' represents the column measurements from MUCCnet and the green '+' stands for the modelled $\mathrm{XCH}_{4,\mathrm{sla}}^{\mathrm{S}}$. The other curves in the plot show the modelled column concentrations calculated following Eq.1 of the main text, i.e. without smoothing using the SZA-dependent AK: black curve – modelled background ($\mathrm{XCH_4}$_BCK); red curve – modelled $\mathrm{XCH_4}$. The dashed yellow and blue curves highlight the concentration changes caused by human activities ($\mathrm{XCH_4}$_ANT) and biogenic activities ($\mathrm{XCH_4}$_BIO). The grey shaded areas mark the measurement periods used for comparing to the simulations.

S8 The map of the modelled Net Ecosystem Exchange (NEE)

The maps of the modelled net ecosystem exchange (NEE) for the outermost domain on a sample date (21 August) are plotted in Fig. S7. The southern part of the EU is more biologically active and has greater carbon sinks compared to more northerly regions. As a result, sometimes air masses from the northern part of the EU mix with air masses with less CO_2 (due to the biospheric uptake) from the southern part of the EU near to the Alps, close to Munich and the center of our domain.

S9 Wind roses during the daytime

Figure S9 provides the daytime wind roses (from 6:00 UTC to 17:00 UTC) day by day from 1 to 30 August, 2018. Each wind rose shows wind speeds and wind directions at 30 meter height above the ground at LMU.

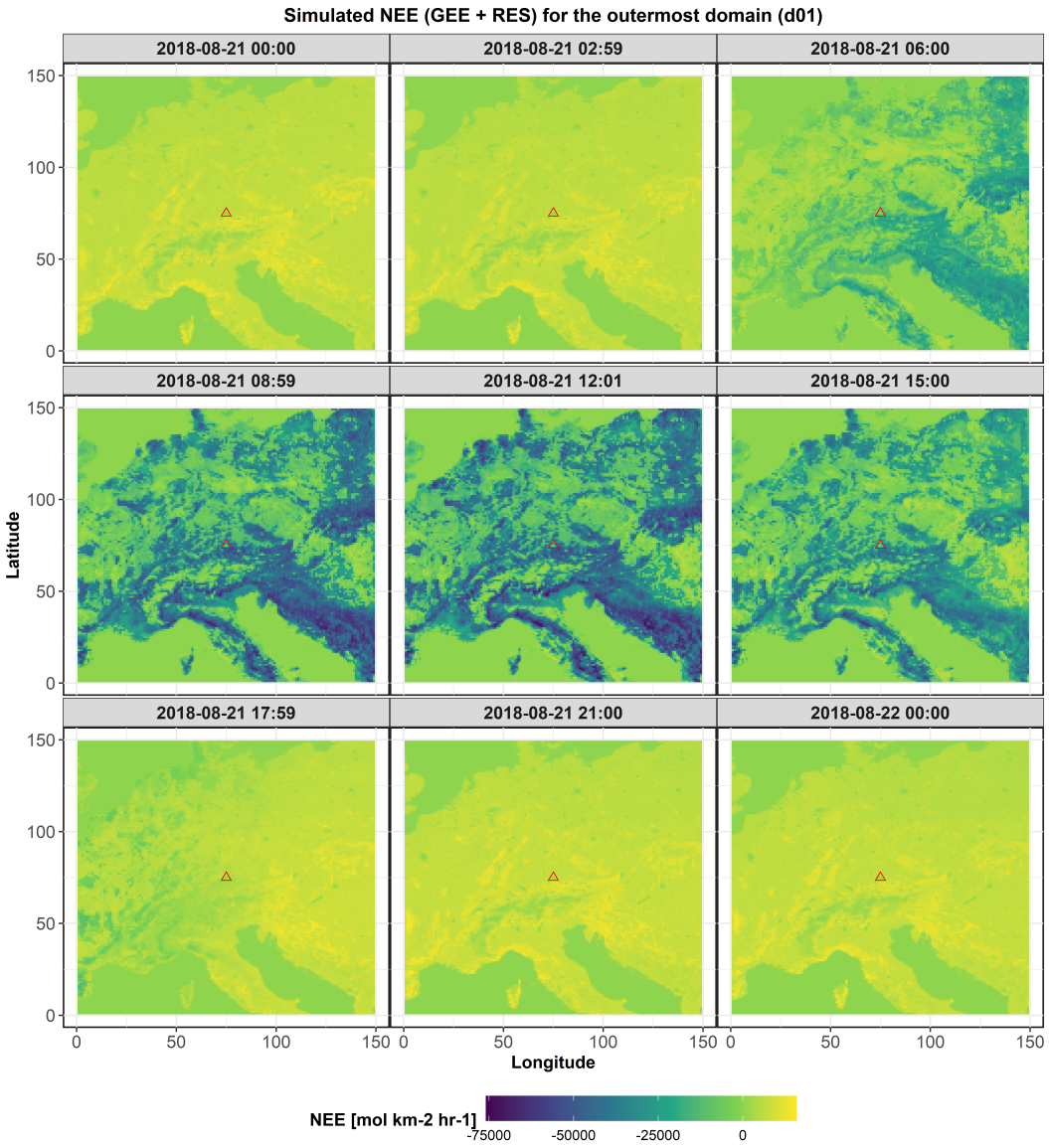

Figure S7. The map of modelled net ecosystem exchange (NEE) on 21 August for the outermost domain (d01).

S10 Definition of footprint percentile contours

To define the percentile contours of STILT footprints used in our study, we performed the following steps: first, the values of the slant column footprint map were ordered and the cumulative sum of these sorted values was calculated (see Fig. S10.(a)); Secondly, based on the plot of the cumulative sum of the sorted values, a threshold under a specific percentile was defined to exclude points with lower sensitivity, e.g., the 90th pecentile (brown line in Fig. S10.(a)); Finally, the footprint contours of the

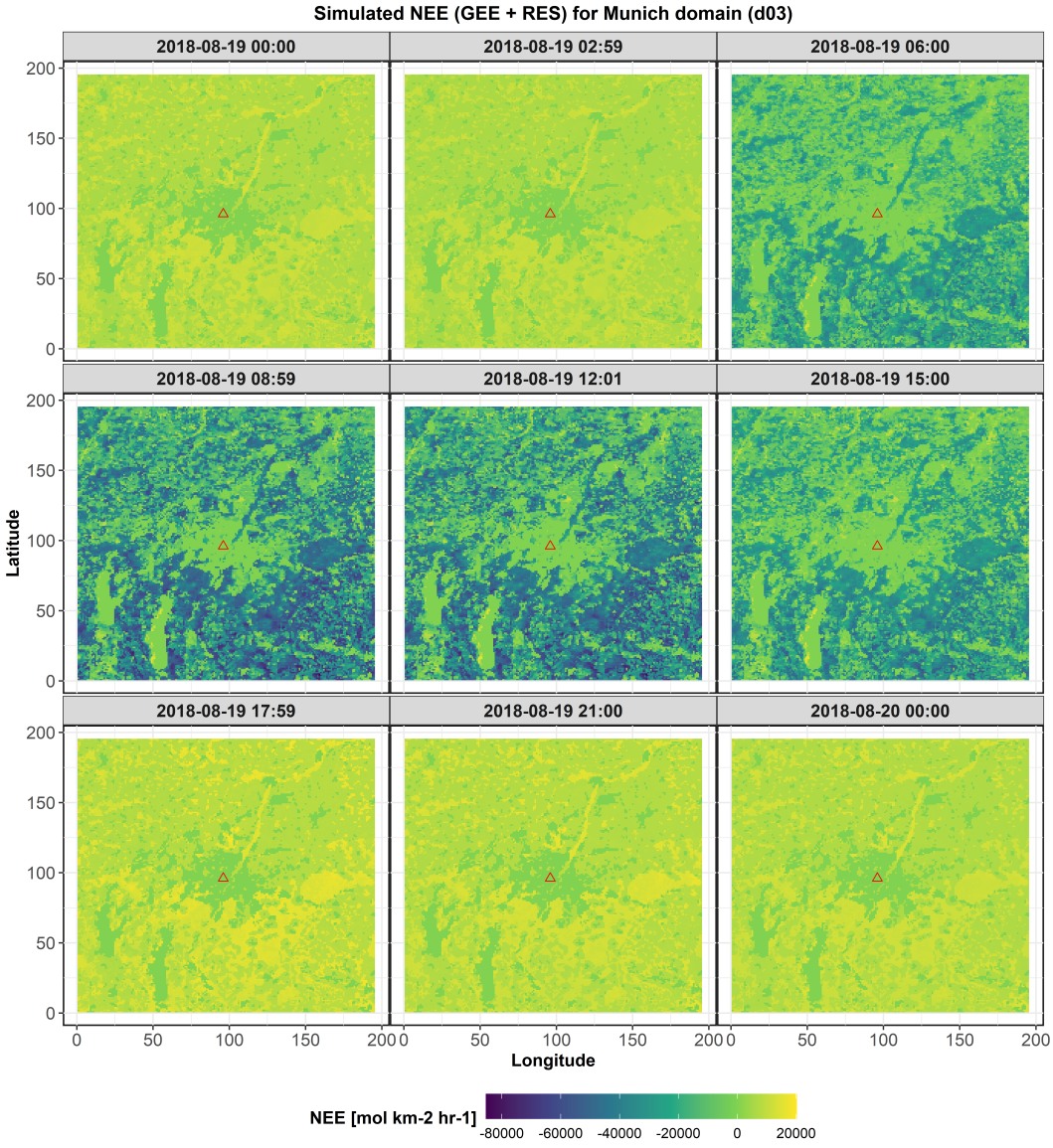

Figure S8. The map of net ecosystem exchange (NEE) on 19 August for the innermost domain (d03), modelled with the VPRM using the new land use categories mentioned in Sect.S2.

different percentiles were defined. The generation of footprint percentile contours in our study is based on the approach used in Dayalu et al. (2020).

Table S5 lists the receptor times used for generating the footprint contours in Fig. S10(b) and Fig. 7. As described in Sect. 5, the receptor time (i.e. the time when the air parcels are released from the receptor backwards in time by STILT) is defined
105 based on the observed peak time. In cases where this observed peak time cannot be read from Figs. 4 and 5, it is defined by

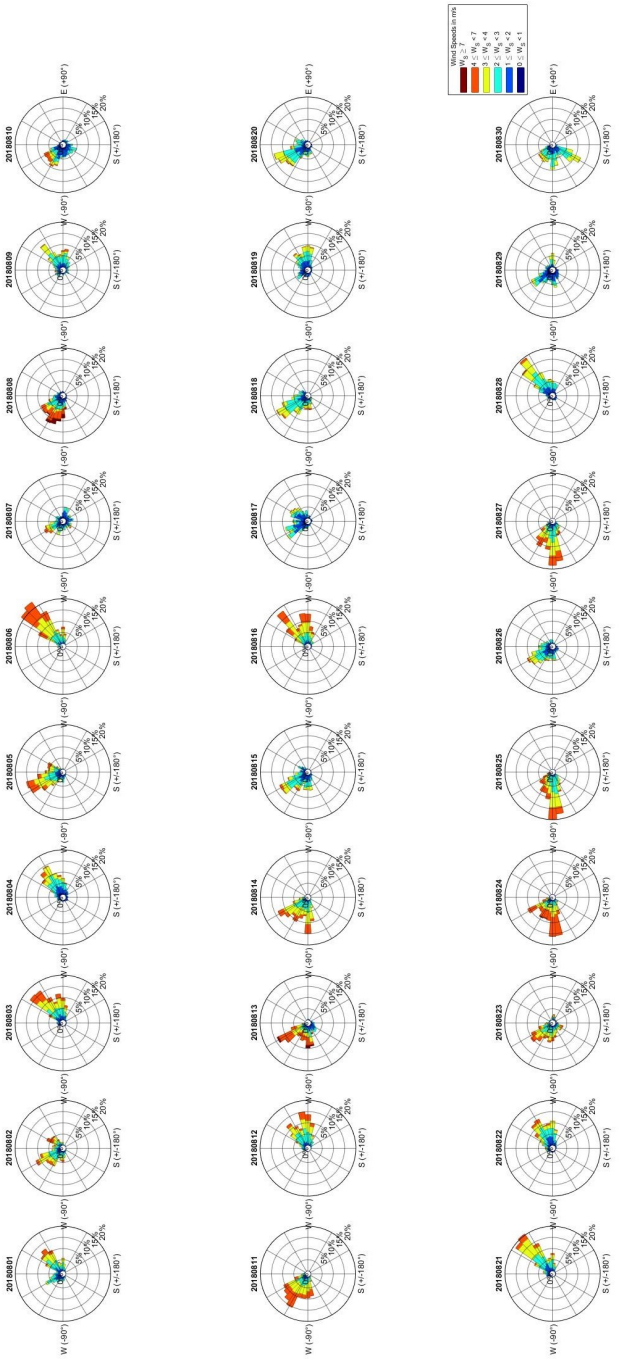

Figure S9. Daytime wind roses, measured day by day at LMU.

considering the peak time at a corresponding upwind site and adding a transport time estimate. However, when Höhenkirchen (south) site was to be regarded as a rather upwind site under Northeasterly/Easterly wind, and the peak time is not readable from the figures, its receptor time (see '-' in Table S5).

Figure S11 shows the footprint contours at the up- and downwind sites from 17 to 21 August, 2018. In our study, footprint contours are generated to show the main area travelled by air parcels released from the receptor, which can also be used to understand the prevailing wind conditions over the domain. A footprint contour generated under steady wind conditions always starts at the receptor and spreads gradually in the direction which the air parcels come from. In contrast, unsteady wind results in the disordered travel of air parcels, making it hard to relate the prevailing wind direction to the footprint contours. In classical DCM, the air masses should theoretically pass by the upwind site and further arrive at the downwind site with a relatively stable wind, after travelling through an urban area in which most of emissions are located. Using our refined DCM approach discussed in the main text, Section 5.3, we can apply DCM for three dates: 16, 20, and 21 August.

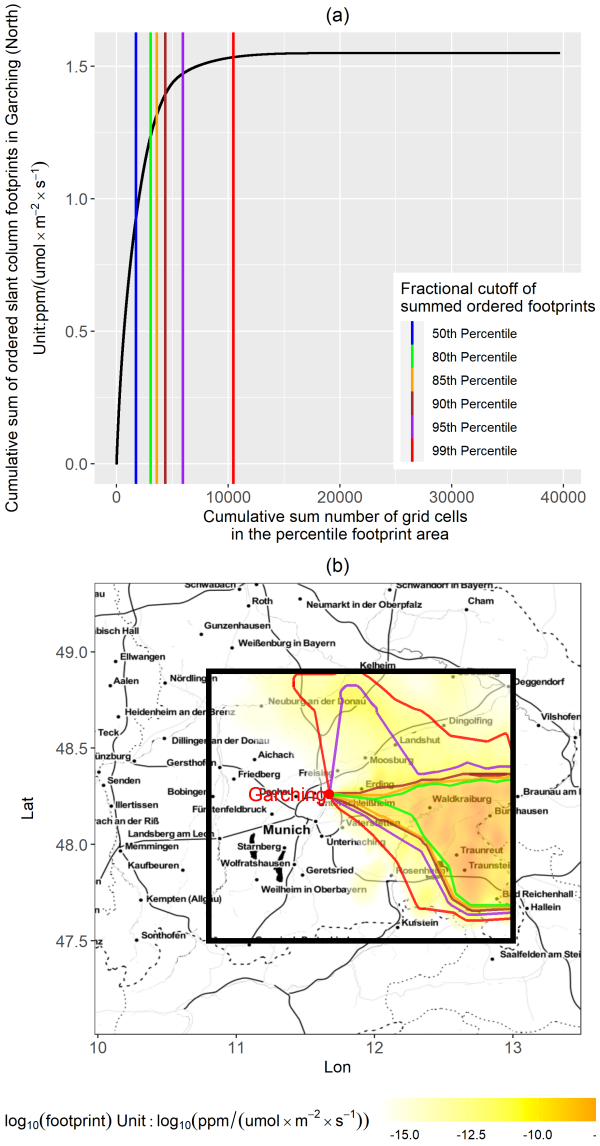

Figure S10. (a) The cumulative contribution of sorted slant column footprints to footprint area and concentration for one sample site and time: Garching at 11 am on 16 August, 2018 (trajectories running backwards for 10 hours). Six percentile thresholds were used for selecting points with footprints at or higher than threshold value. (b) The slant column footprint and its percentile contours: red for the 99th percentile, purple for the 95th percentile, brown for 90th percentile, orange for 85th percentile and green for 80th percentile. @ggmap (Kahle and Wickham, 2013)

Table S1. Mapping the Copernicus classes to SYNMAP classes used in the VPRM prepossessor.

	SYNMAP VPRM Classes							
	Evergreen	Deciduous	Mixed Forest	Shrubland	Savanna	Cropland	Grassland	Others
Copernicus classes	Coniferous forest	Broad-leaved forest	Mixed forest	Moors and heathland	Beaches-dunes-sands	Rice fields	Natural grasslands	Continuous urban fabric
	-	-	-	Sclerophyllous vegetation	Bare rocks	Vineyards	Pastures	Discontinuous urban fabric
	-	-	-	Transitional woodland-shrub	Sparsely vegetated areas	Fruit trees and berry plantations	Green urban areas	Industrial or commercial units
	-	-	-	-	-	Olive groves	-	Road and rail networks and associated land
	-	-	-	-	-	Annual crops associated with permanent crops	-	Port areas
	-	-	-	-	-	Non-irrigated arable land	-	Airports
	-	-	-	-	-	Complex cultivation patterns	-	Construction site
	-	-	-	-	-	Complex cultivation patterns	-	Construction site
	-	-	-	-	-	Land principally occupied by agriculture with significant areas of natural vegetation	-	Sport and leisure facilities
	-	-	-	-	-	Agro-forestry areas	-	Glaciers and perpetual snow
	-	-	-	-	-	-	-	Water courses
	-	-	-	-	-	-	-	Water bodies
	-	-	-	-	-	-	-	Coastal lagoons
	-	-	-	-	-	-	-	Sea and ocean
	-	-	-	-	-	-	-	NODATA
	-	-	-	-	-	-	-	Mineral extraction sites
	-	-	-	-	-	-	-	Dump sites
	-	-	-	-	-	-	-	Permanently irrigated land
	-	-	-	-	-	-	-	Inland marshes
	-	-	-	-	-	-	-	Peat bogs
	-	-	-	-	-	-	-	Salt marshes
	-	-	-	-	-	-	-	Salines
	-	-	-	-	-	-	-	Intertidal flats
	-	-	-	-	-	-	-	Estuaries
	-	-	-	-	-	-	-	Burnt areas

Table S2. Aggregation of emission categories for CO_2 from GNRF to our model.

GNFR	Categories in WRF for CO_2				
	A. Power Plants	B. Industry	C. Other Stationary Combustion	D. Road Transport	E. Others
A:Public power	■				
B:Industry		■			
C:Other stationary combustion			■		
D:Fugitives					■
E:Solvents					■
F:Road transport				■	
G:Shipping					■
H:Aviation					■
I:Offroad					■
J:Waste					■
K&L: Agriculture (Livestock & others)					■

Table S3. Aggregation of emission categories for CH_4 from GNRF to our model.

GNFR	Categories in WRF for CH_4					
	A. Power Plants	B. Industry	C. Agriculture	D. Waste Management	E. Fugitives and solvents	F. Others
A:Public power	■					
B:Industry		■				
C:Other stationary combustion						■
D:Fugitives					■	
E:Solvents					■	
F:Road transport						■
G:Shipping						■
H:Aviation						■
I:Offroad						■
J:Waste				■		
K&L: Agriculture (Livestock & others)			■			

Table S4. Summary of day-by-day measurement performance from 1 to 30, August in 2018 at our five measurement sites, including the number of measurement points for each site, overall data coverage for each measurement date (with the classifications from poor to excellent: +, ++, +++, ++++) based on the available observations, averaged wind speeds during the day time, and wind directions at the ground level obtained from the LMU stations (Hase et al., 2015; Vogel et al., 2019)

Date	Quality	Number of Observations					Wind Speed	Wind Direction
		Garching (North)	TUM (Center)	Höhenkirchen (South)	Markt Schwaben (East)	Weßling (West)		
20180801 (Wed)	+	15	127	0	0	0	2.56	W-N-E
20180802 (Thu)	+	0	131	0	0	35	2.92	W-N-E
20180803 (Fri)	+	28	137	82	0	50	2.70	W-N-E
20180804 (Sat)	++++	127	131	125	125	60	2.11	N-E
20180805 (Sun)	++++	110	131	82	99	68	2.83	NW-NE
20180806 (Mon)	+++	114	126	124	126	88	3.19	NE
20180807 (Tue)	+	0	47	0	53	23	2.10	W-N-SE
20180808 (Wed)	++	89	92	76	106	37	3.30	W-N
20180809 (Thu)	++++	112	97	106	106	130	2.49	SE-N
20180810 (Fri)	+	0	0	0	0	0	2.19	N-W-S
20180811 (Sat)	+++	100	93	91	114	99	3.29	W
20180812 (Sun)	+	130	0	135	135	136	2.68	E-N
20180813 (Mon)	+	73	81	72	93	68	3.10	W-N-W
20180814 (Tue)	+	0	0	0	0	0	3.16	NW
20180815 (Wed)	+	57	94	0	89	46	2.26	SW-N-NE
20180816 (Thu)	++++	110	133	105	133	133	2.97	E-NE
20180817 (Fri)	+++	102	130	131	132	97	1.87	W-N-E
20180818 (Sat)	+++	75	69	100	98	71	2.56	NW
20180819 (Sun)	++++	127	130	129	132	127	2.03	W-N
20180820 (Mon)	++++	126	127	126	131	112	2.25	W-N
20180821 (Tue)	+++	109	131	115	130	109	2.44	NW-N-E
20180822 (Wed)	++++	129	130	128	130	129	2.26	N-E
20180823 (Thu)	++	60	102	75	72	72	3.14	W-N-S
20180824 (Fri)	+	0	0	0	0	0	3.79	W
20180825 (Sat)	+	0	0	0	0	0	3.16	W
20180826 (Sun)	+	23	83	28	0	0	2.28	W-N-E
20180827 (Mon)	+++	81	75	98	101	61	2.95	W
20180828 (Tue)	+++	66	72	104	99	75	2.18	NE
20180829 (Wed)	+++	79	86	55	86	94	1.71	SW-N-E
20180830 (Thu)	+	0	0	0	0	0	2.52	W

Table S5. List of receptor times for our five measurement sites from 18 to 22 August, 2018.

Date	Receptor time (UTC)				
	Garching (North)	Markt Schwaben (East)	TUM (Center)	Weßling (West)	Höhenkirchen (South)
20180816	11:00	11:00	12:00	14:00	11:30
20180817	11:00	11:00	13:00	11:00	15:00
20180818	11:00	11:00	12:00	14:00	11:00
20180819	11:00	12:00	11:00	15:00	11:30
20180820	13:00	13:00	12:00	9:00	13:00
20180821	10:30	11:00	12:00	14:30	-
20180822	13:00	11:00	12:00	15:30	-

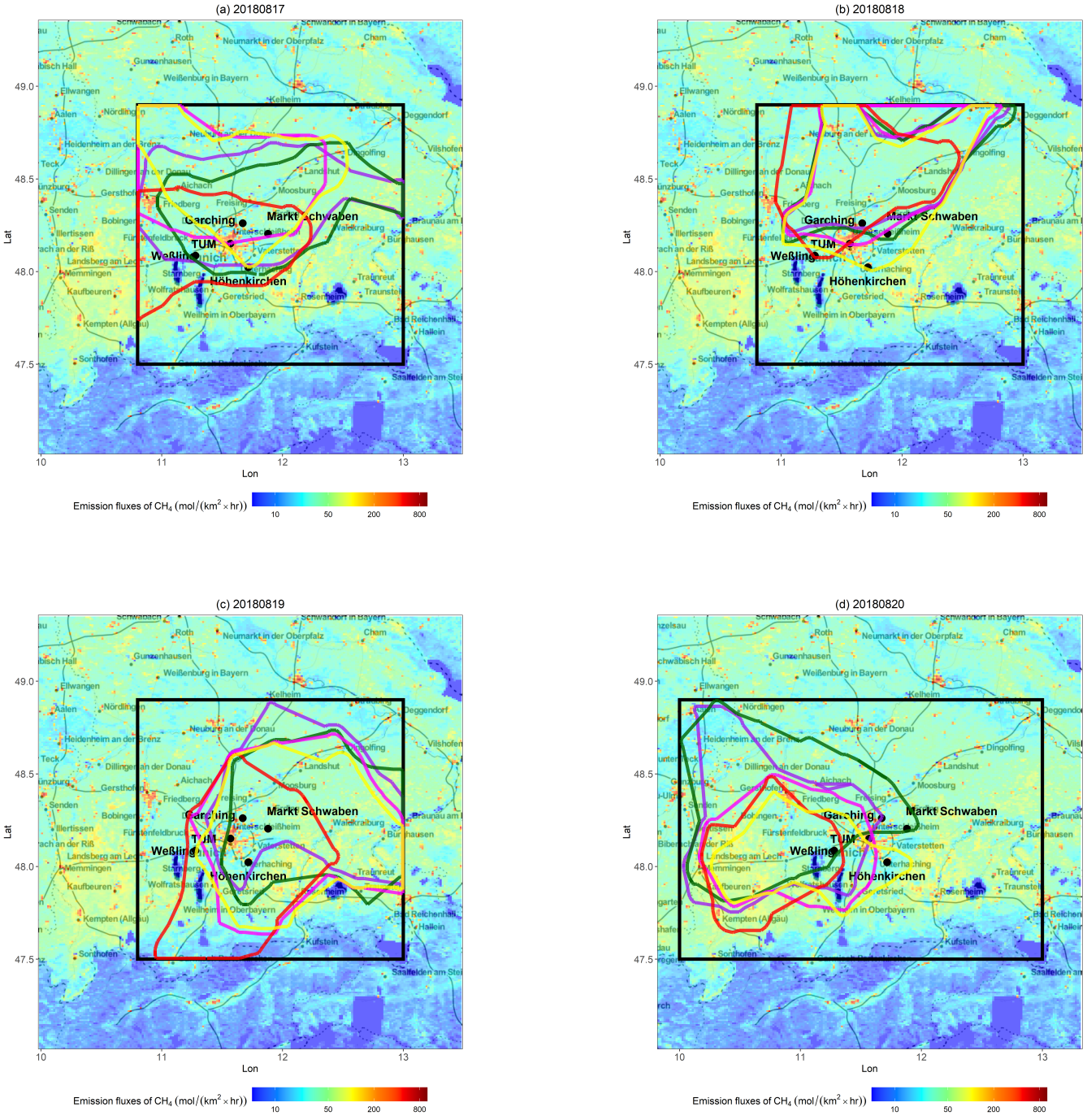
(a) 20180817
(b) 20180818
(c) 20180819
(d) 20180820
Garching
Markt Schwaben
TUM
Weßling
Höhenkirchen
Lat
Lon
Emission fluxes of CH4 (mol/(km2 × hr))
10
50
200
800

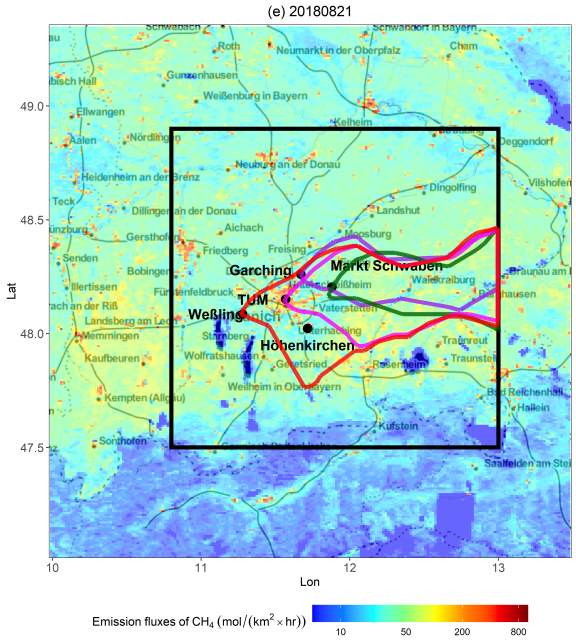

Figure S11. Footprint contours from 18 to 21 August at up- and downwind sites with different colors: red for Weßling (West), green for Markt Schwaben (East), purple for Garching (North) and pink for TUM (Center), yellow for Höhenkirchen (South). @ggmap (Kahle and Wickham, 2013)

References

Bieser, J., Aulinger, A., Matthias, V., Quante, M., and Van Der Gon, H. D.: Vertical emission profiles for Europe based on plume rise calculations, Environmental Pollution, 159, 2935–2946, https://doi.org/10.1016/j.envpol.2011.04.030, 2011.

Brousse, O., Martilli, A., Foley, M., Mills, G., and Bechtel, B.: WUDAPT, an efficient land use producing data tool for mesoscale models? Integration of urban LCZ in WRF over Madrid, Urban Climate, 17, 116–134, https://doi.org/10.1016/j.uclim.2016.04.001, 2016.

Browne, P. A., de Rosnay, P., Zuo, H., Bennett, A., and Dawson, A.: Weakly coupled ocean–atmosphere data assimilation in the ECMWF NWP system, Remote Sensing, 11, 234, https://doi.org/10.3390/rs11030234, 2019.

Collier, E., Mölg, T., Maussion, F., Scherer, D., Mayer, C., and Bush, A.: High-resolution interactive modelling of the mountain glacier–atmosphere interface: an application over the Karakoram, The Cryosphere, 7, 779–795, https://doi.org/10.5194/tc-7-779-2013, 2013.

Dayalu, A., Munger, J. W., Wang, Y., Wofsy, S. C., Zhao, Y., Nehrkorn, T., Nielsen, C., McElroy, M. B., and Chang, R.: Evaluating China's anthropogenic CO_2 emissions inventories: a northern China case study using continuous surface observations from 2005 to 2009, Atmospheric Chemistry and Physics, 20, 3569–3588, https://doi.org/10.5194/acp-20-3569-2020, 2020.

Demuzere, M., Bechtel, B., Middel, A., and Mills, G.: Mapping Europe into local climate zones, PloS one, 14, e0214 474, https://doi.org/10.1371/journal.pone.0214474, 2019.

Friedl, M. A., Sulla-Menashe, D., Tan, B., Schneider, A., Ramankutty, N., Sibley, A., and Huang, X.: MODIS Collection 5 global land cover: Algorithm refinements and characterization of new datasets, Remote sensing of Environment, 114, 168–182, https://doi.org/10.1016/j.rse.2009.08.016, 2010.

Hase, F., Frey, M., Blumenstock, T., Groß, J., Kiel, M., Kohlhepp, R., Mengistu Tsidu, G., Schäfer, K., Sha, M., and Orphal, J.: Application of portable FTIR spectrometers for detecting greenhouse gas emissions of the major city Berlin, Atmospheric Measurement Techniques, 8, 3059–3068, https://doi.org/10.5194/amt-8-3059-2015, 2015.

Hersbach, H., Bell, B., Berrisford, P., Hirahara, S., Horányi, A., Muñoz-Sabater, J., Nicolas, J., Peubey, C., Radu, R., Schepers, D., et al.: The ERA5 global reanalysis, Quarterly Journal of the Royal Meteorological Society, 146, 1999–2049, https://doi.org/10.1002/qj.3803, 2020.

Kahle, D. and Wickham, H.: ggmap: Spatial Visualization with ggplot2, The R Journal, 5, 144–161, https://journal.r-project.org/archive/2013-1/kahle-wickham.pdf, 2013.

Mahadevan, P., Wofsy, S. C., Matross, D. M., Xiao, X., Dunn, A. L., Lin, J. C., Gerbig, C., Munger, J. W., Chow, V. Y., and Gottlieb, E. W.: A satellite-based biosphere parameterization for net ecosystem CO_2 exchange: Vegetation Photosynthesis and Respiration Model (VPRM), Global Biogeochemical Cycles, 22, https://doi.org/10.1029/2006GB002735, 2008.

Rémy, S., Kipling, Z., Flemming, J., Boucher, O., Nabat, P., Michou, M., Bozzo, A., Ades, M., Huijnen, V., Benedetti, A., et al.: Description and evaluation of the troposphere aerosol scheme in the European Centre for Medium-Range Weather Forecasts (ECMWF) Integrated Forecasting System (IFS-AER, cycle 45R1), Geoscientific Model Development, 12, 4627–4659, https://doi.org/10.5194/gmd-12-4627-2019, 2019.

See, L., Perger, C., Duerauer, M., Fritz, S., Bechtel, B., Ching, J., Alexander, P., Mills, G., Foley, M., O'Connor, M., et al.: Developing a community-based worldwide urban morphology and materials database (WUDAPT) using remote sensing and crowdsourcing for improved urban climate modelling, in: 2015 Joint Urban Remote Sensing Event (JURSE), pp. 1–4, IEEE, https://doi.org/10.1109/JURSE.2015.7120501, 2015.

Super, I., Dellaert, S. N., Visschedijk, A. J., and Denier van der Gon, H. A.: Uncertainty analysis of a European high-resolution emission inventory of CO_2 and CO to support inverse modelling and network design, Atmospheric Chemistry and Physics, 20, 1795–1816, https://doi.org/10.5194/acp-20-1795-2020, 2020.

Vogel, F. R., Frey, M., Staufer, J., Hase, F., Broquet, G., Xueref-Remy, I., Chevallier, F., Ciais, P., Sha, M. K., Chelin, P., et al.: XCO_2 in an emission hot-spot region: the COCCON Paris campaign 2015, Atmospheric Chemistry and Physics, 19, 3271–3285, https://doi.org/10.5194/acp-19-3271-2019, 2019.